Feasibility study of a proton CT system based on 4D-tracking and residual energy determination via time-of-flight

Felix Ulrich-Pur, Thomas Bergauer, Alexander Burker, Albert Hirtl, Christian Irmler, Stefanie Kaser, Florian Pitters, Simon Rit

Feasibility study of a proton CT system based on 4D-tracking and residual energy determination via time-of-flight

Felix Ulrich-Pur[1], Thomas Bergauer[1], Alexander Burker[2], Albert Hirtl[2], Christian Irmler[1], Stefanie Kaser[1], Florian Pitters[1], Simon Rit[3]

[1] Austrian Academy of Sciences, Institute of High Energy Physics (HEPHY), Nikolsdorfer Gasse 18, 1050 Wien, Austria

[2] TU Wien, Atominstitut, Stadionallee 2, 1020 Wien, Austria

[3] Lyon University, INSA-Lyon, University Lyon1, UJM-Saint Etienne, CNRS, Inserm, CREATIS UMR5220, U1206, France

E-mail: felix.ulrich-pur@oeaw.ac.at

March 2022

Abstract.

Objective For dose calculations in ion beam therapy, it is vital to accurately determine the relative stopping power (RSP) distribution within the treatment volume. A suitable imaging modality to achieve the required RSP accuracy is proton computed tomography (pCT), which usually uses a tracking system and a separate residual energy (or range) detector to directly measure the RSP distribution. This work investigates the potential of a novel pCT system based on a single detector technology, namely low gain avalanche detectors (LGADs). LGADs are fast 4D-tracking detectors, which can be used to simultaneously measure the particle position and time with precise timing and spatial resolution. In contrast to standard pCT systems, the residual energy is determined via a time-of-flight (TOF) measurement between different 4D-tracking stations.

Approach To show the potential of using 4D-tracking for proton imaging, we studied and optimized the design parameters for a realistic TOF-pCT system using Monte Carlo simulations. We calculated the RSP accuracy and RSP resolution inside the inserts of the CTP404 phantom and compared the results to a simulation of an ideal pCT system.

Main results After introducing a dedicated calibration procedure for the TOF calorimeter, RSP accuracies less than 0.6 % could be achieved. We also identified the design parameters with the strongest impact on the RSP resolution and proposed a strategy to further improve the image quality.

Significance This comprehensive study of the most important design aspects for a novel TOF-pCT system could help guide future hardware developments and, once implemented, improve the quality of treatment planning in ion beam therapy.

Time-of-flight, 4D-tracking detector, low gain avalanche detectors, proton computed tomography, proton therapy, RSP accuracy, RSP precision
Submitted to: *Phys. Med. Biol.*

1. Introduction

In recent years, several 4D-tracking detectors, i.e. particle detectors that allow the simultaneous measurement of the particle's position and time, have emerged from the rising demand for particle trackers able to cope with the increasing luminosity in high energy physics experiments such as ATLAS, CMS or HADES [1, 2, 3]. Low gain avalanche detectors (LGADs), for example, are widely studied and used [4] since they have high rate-capabilities, they offer timing resolutions in the order of $30 - 50\,\mathrm{ps}$ [3, 5] and, depending on the LGAD technology, can have spatial resolutions down to few tens of µm [6, 7]. Due to the growing interest in this detector technology, LGADs have been continuously advancing, making 4D-tracking also very attractive for other applications such as ion imaging, e.g. proton computed tomography (pCT) [8].
Proton computed tomography is an imaging modality that aims at improving the treatment planning accuracy for ion beam therapy [9] by directly measuring the relative stopping power (RSP) distribution within the patient, i.e. energy loss per unit path length expressed relative to water. In conventional pCT, the RSP is obtained by estimating the particle path and deposited energy inside the traversed object via a tracking system and a separate residual range or residual energy detector placed downstream of the tracking system. Even though several promising pCT prototypes [10, 11, 12, 13] have been developed in recent years, most of the pCT scanners still struggle with the demanding data rate requirements of a clinical system [14]. According to [14], a pCT system suitable for clinical use should reach data acquisition rates of at least a few MHz in order to keep the acquisition time of a full pCT scan comparable to a standard CT scan ($< 1\,\mathrm{min}$), while, at the same time, it should achieve RSP accuracies $\leq 1\,\%$ with a spatial resolution $\leq 1\,\mathrm{mm}$. Fulfilling all of the previously mentioned clinical requirements, while keeping the production and maintenance costs as well as the system's complexity as low as possible proves to be a formidable task.
A promising solution, which addresses all those challenges at once, is the development of an LGAD-based pCT scanner that uses 4D-tracking for both the particle path estimation and the residual energy determination via time-of-flight (TOF) measurements [15]. Employing 4D-tracking detectors would not only help to boost the data rate capability of the imaging system, but it also opens up the possibility of integrating the TOF through the patient into the imaging process, e.g. by combining the energy loss inside the patient with the corresponding TOF to filter nuclear events [16]. However, since this would go beyond the scope of this study, we mainly focus on the TOF-based residual energy measurement.
Although the concept of using a TOF calorimeter for ion imaging has already been

explored by [17] and [18], no systematic analysis of a realistic pCT system based on 4D-tracking detectors that could potentially meet all clinical requirements has been performed so far. Therefore, within this study, we present a comprehensive feasibility study of an LGAD-based pCT system, which should serve as a guide for future hardware developments. For that purpose, the influence of various detector design aspects on the performance of the TOF-pCT scanner has been studied and is presented in two parts. First, the impact of different system parameters of a stand-alone TOF calorimeter on the energy resolution and accuracy of the residual energy measurement is explored. Also, a dedicated calibration procedure for the TOF calorimeter is presented. Second, the performance of an LGAD-based TOF-pCT system using the same detector technology for particle tracking and residual energy determination is investigated. The RSP accuracy and precision are measured using the CTP404 phantom and are then compared to the results of the latest pCT scanner [19].

2. Materials and methods

To assess the performance of the investigated pCT systems based on 4D-tracking detectors, Monte Carlo (MC) simulations of realistic TOF-pCT systems were performed and compared to simulations of an ideal pCT setup, without a TOF calorimeter and with ideal energy and position measurement. All pCT setups were modeled in Geant4 (version 10.05.1) [20] using the *QGSP_BIC_EMY* physics list with *EM_Options 3*.

2.1. Time-of-flight calorimeter

First, basic design choices for the TOF-pCT system were made based on separate MC simulations of a realistic stand-alone TOF calorimeter. To estimate the performance of each of the investigated calorimeter settings, the energy resolution and absolute error were determined as a measure for precision and accuracy.

2.1.1. Setup geometry

A schematic drawing of the simulated setup is depicted in figure 1. The TOF calorimeter was simulated using two timing stations, each consisting of n=2 4D-tracking planes, placed 10 cm apart (D_1=D_2=10 cm). To create a realistic model of a TOF calorimeter, each tracking plane was modelled as a generic LGAD module, consisting of a silicon layer (Si) for the sensor and a copper (Cu) and flame retardant glass epoxy (FR4) layer to model a printed circuit board (PCB). The thickness X of each material inside an LGAD plane (X^{Si}, X^{Cu}, X^{FR4}) was then varied to simulate different detector technologies (e.g. strip sensors or pixel detectors). To compare the material composition of different detector technologies, the material budget [21] per tracking plane was calculated using

$$\epsilon = \sum_i \frac{X^i}{X_0^i} = \frac{X^{Si}}{X_0^{Si}} + \frac{X^{Cu}}{X_0^{Cu}} + \frac{X^{FR4}}{X_0^{FR4}}. \quad (1)$$

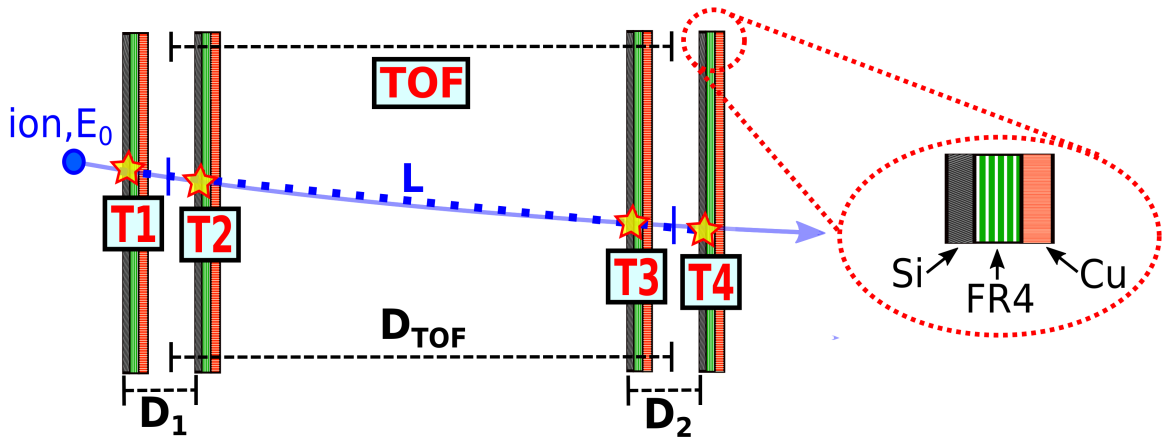

Figure 1: Schematic of a TOF calorimeter based on LGAD detectors. The TOF is measured between two timing stations (T1/T2 and T3/T4), each consisting of two generic LGAD planes, modelled as a silicon (Si), copper (Cu) and flame retardant glass epoxy (FR4) compound (the cross section of an LGAD plane is depicted on the right). A straight line fit through all hit positions (x_i, y_i) is used to estimate the flight path length L (dotted line).

The radiation lengths for Si (X_0^{Si}=93.7 mm) and copper (X_0^{Cu}=14.36 mm) were extracted from [22] and FR4 (X_0^{FR4}=167.608 mm) from [23]. Standard LGAD sensors typically consist of a 300-350 µm thick silicon layer [24], which corresponds to a material budget of $\approx$ 0.32-0.37 % X/X_0. Depending on the detector technology, the silicon sensor can also be mounted on a PCB. For example, the LGAD pad detectors, as described in [5] were mounted on the USCS readout board [25] and had a total material budget of $\approx$ 2 % X/X_0. Within our studies, three different material budgets were simulated (0.1 %, 1 % and 2.3 % X/X_0) to cover a larger range of possible values. 0.1 % X/X_0 and 2.3 % X/X_0 are more extreme examples and correspond to a single 100 µm silicon layer and a compound consisting of a 300 µm silicon, 200 µm copper and 1 mm FR4 layer.
To model the intrinsic spatial and timing resolution of a realistic LGAD sensor, the transversal hit position (x_i, y_i) and the hit time T_i at sensor i were blurred using a Gaussian distribution with a standard deviation of σ_{xy} and σ_T, respectively. For all settings, the spatial resolution σ_{xy} was varied between 0 and 5 mm to study the influence of the spatial granularity of different sensor geometries. Also different intrinsic time resolutions σ_T, ranging from 0 to 100 ps were investigated.

2.1.2. Residual energy determination via time-of-flight measurements
For the TOF-based energy measurement, the mean hit time per timing station was used to calculate the TOF through the calorimeter according to

$$\mathrm{TOF} = \frac{1}{n}\left(\sum_{i}^{n} T_{i+n} - T_i\right), \tag{2}$$

with $n = 2$ LGADs/timing station. Assuming a constant velocity v along the particle

path inside the TOF calorimeter, the kinetic energy of each particle with mass m_0 was calculated as follows

$$E_{\text{kin}} = m_0 c^2 \cdot \left(\frac{1}{\sqrt{1 - \frac{v^2}{c^2}}} - 1 \right), \tag{3}$$

using $v \approx L/\text{TOF}$, where L is the flight path length (figure 1) and TOF is the time-of-flight as defined in equation (2). For the path length estimation, a straight-line fit through all hit positions (x_i, y_i) along the particle's path was used (dotted line in figure 1). The distance between the points on the resulting straight line, located at the centre between each timing station, was used to calculate the flight path length L.
To study the influence of the TOF calorimeter length, the flight distance D_{TOF} was varied between 0.5 and 1.5 m. The performance of each calorimeter setting was tested using 1×10^5 primary protons with kinetic energies ranging from 50 to 400 MeV.

2.1.3. Precision of the residual energy measurement

To estimate the precision of the residual energy measurement, the energy resolution $\sigma_{E_{\text{meas}}}/E_{\text{meas}}$, was determined via simulation for each setting. In addition, the theoretical energy resolution was calculated using first order Gaussian error propagation (GEP) of equation (3)

$$\frac{\sigma_{E_{\text{kin}}}}{E_{\text{kin}}} = \frac{1}{E_{\text{kin}}} \cdot \sqrt{\left(\frac{\partial E_{\text{kin}}}{\partial \text{TOF}} \cdot \sigma_{\text{TOF}} \right)^2 + \left(\frac{\partial E_{\text{kin}}}{\partial L} \cdot \sigma_L \right)^2}. \tag{4}$$

The resulting theoretical energy resolution

$$\frac{\sigma_{E_{\text{kin}}}}{E_{\text{kin}}} = \frac{\gamma^3 \beta^2}{L\,(\gamma - 1)} \sqrt{{\sigma_{\text{TOF}}}^2 \beta^2 c^2 + {\sigma_L}^2}, \tag{5}$$

with $\gamma = 1/\sqrt{1 - \beta^2}$ and $\beta = v/c$, is equivalent to the energy resolution described in [18], if no path length uncertainty ($\sigma_L = 0$) is assumed. To calculate the uncertainty of the total TOF (σ_{TOF}), a GEP of equation (2) was performed, resulting in

$$\sigma_{\text{TOF}} = \sqrt{\sum_i^{2n} \left(\frac{\partial \text{TOF}}{\partial \text{T}_i} \cdot \sigma_{\text{T}_i} \right)^2} = \sqrt{\frac{2}{n}} \cdot \sigma_{\text{T}}. \tag{6}$$

Since the same intrinsic time resolution per LGAD was assumed ($\sigma_{\text{T}_i} = \sigma_{\text{T}}$) and two LGADs were used per timing station ($n = 2$), the theoretical uncertainty of the TOF is equivalent to the intrinsic time resolution per plane. For each setting, the energy resolution was obtained from a simulation of a realistic setup and compared to the theoretical energy resolution (equation (5)).

2.1.4. Accuracy and calibration of a realistic TOF calorimeter

In section 2.1.2 and section 2.1.3, the energy loss of ions along their path through the TOF calorimeter was neglected. However, since the investigated setup is placed in air and consists of multiple LGAD detectors mounted on a PCB, a significant energy

loss is expected. Therefore, to improve the accuracy of the energy measurement, it is essential to account for the energy loss along the particle's trajectory and to apply a suitable energy calibration. Also, the intrinsic time resolution has to be considered in the calibration since the non-linear relation between TOF and kinetic energy (equation (3)) affects the energy measurement if realistic intrinsic time resolutions ($\geq 30\,\mathrm{ps}$) are assumed. To show this effect, the theoretical TOF was calculated for 800 MeV protons and distorted using a Gaussian distribution with a standard deviation of σ_{TOF} emulating an uncertainty of the TOF measurement while neglecting the energy loss along the flight path. However, for a realistic TOF calorimeter, both energy loss and intrinsic time resolution have to be taken into account. To quantify the corresponding systematic error of the energy measurement, the absolute error

$$\Delta E = E_{\mathrm{meas}} - E_{\mathrm{in}} \tag{7}$$

was calculated for each setting, with E_{meas} as the measured kinetic energy and E_{in} as the primary beam energy, which was varied between 50 and 400 MeV. For the calibration, ΔE was approximated by an empirical model

$$f(E,\vec{\theta}) = \frac{(E-\theta_0)^{1-\theta_1}}{\theta_2} - m_0 c^3 \gamma(E)^3 \beta(E)^2 \left(\frac{\theta_3}{c} - \beta(E)\cdot\theta_4\right), \tag{8}$$

which was fitted to the observed absolute errors of the energy measurement. $\vec{\theta}$, E, $\gamma(E)$, c, m_0 and $\beta(E)$ correspond to the fit parameters, energy, Lorentz-factor, speed of light, proton rest mass and velocity relative to c, respectively. The first part of equation (8) is based on the energy loss of a particle in a homogeneous medium. In general, the total energy loss inside a realistic TOF calorimeter is more complicated since it is the result of multiple energy losses at different parts of the calorimeter, which strongly depends on the setup geometry. The second part is a 2D Taylor expansion of equation (3) to account for inaccuracies in the TOF and path length estimation. However, it has to be mentioned that the calibration curve in equation (8) is not an exact analytical model of the absolute error of the energy measurement, but provides a robust parametrization of the calibration curves for all investigated detector geometries. The resulting calibration curves $f(E)$ were used for all following simulations to correct the inaccuracies of the energy measurement as follows

$$E_{\mathrm{in}}\left(E_{\mathrm{meas}}\right) \approx E_{\mathrm{meas}} + f\left(E_{\mathrm{meas}},\vec{\theta}\right). \tag{9}$$

After applying the calibration according to equation (9), the relative error

$$\epsilon_E = |E_{\mathrm{in}} - E_{\mathrm{meas}}|/E_{\mathrm{in}} \tag{10}$$

was calculated for each setting to estimate the accuracy of the energy measurement.

2.2. Proton computed tomography with 4D tracking detectors

2.2.1. Experimental setup

After simulating a stand-alone TOF calorimeter (see section 2.1), a full pCT system

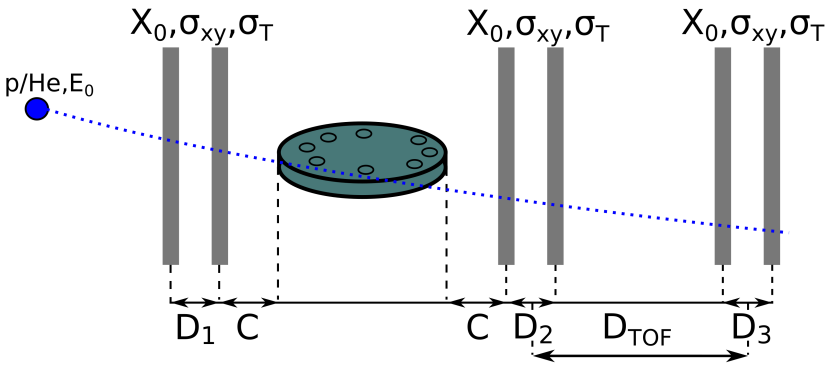

Figure 2: Schematic overview of the simulated pCT setup based on 4D tracking detectors. The performance of the proposed pCT system was studied for different system parameters using the CTP404 phantom.

based on 4D tracking detectors was modelled in Geant4 (figure 2). Different system parameters, as described in table 1, were varied and optimized to design a pCT system that could potentially fulfil the clinical requirements as defined in [14]. In contrast to the stand-alone TOF calorimeter, the intrinsic spatial resolution σ_{xy} of the 4D tracking detectors was set to zero for the TOF-pCT system, which is explained in section 3.1.3. For each setup geometry, a calibration of the TOF calorimeter was performed prior to the pCT measurement (equation (9)). The energy loss inside the first two tracking planes was calculated to correct the primary beam energy E_0, which is needed for the reconstruction.

parameter	**name**	**simulated values**
$\mathbf{X/X_0}$	material budget	0.1, 1, 2.3 %
$\boldsymbol{\sigma_{xy}}$	spatial resolution	0 µm
$\boldsymbol{\sigma_T}$	time resolution per tracking plane	0, 10, 30, 50, 100 ps
$\mathbf{C}$	phantom clearance	10 cm
$\mathbf{D_{1,2,3}}$	distance between tracking planes	10 cm
$\mathbf{D_{TOF}}$	flight distance	50, 100, 150, 200 cm
$\mathbf{E_0}$	beam energy	200, 250, 300, 350, 400 MeV

Table 1: Summary of the varied system parameters to study the overall performance of the TOF-pCT system.

2.2.2. Phantom

In order to compare the results of the proposed TOF-pCT system to the latest pCT scanners, the same phantom as in [19] was used to measure the performance in terms of RSP accuracy and precision. As depicted in figures 2 and 3, the CTP404 phantom is a cylindrical PMMA phantom with a diameter of 15 cm and a thickness of 2.5 cm.

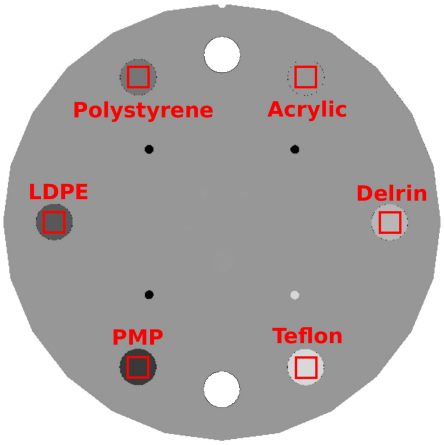

Figure 3: The CTP404 phantom was used to study the performance of the proposed pCT system. The RSP was measured at six different inserts using square-shaped ROIs, highlighted as red squares in this figure.

Inside the PMMA cylinder, inserts with different materials, shapes and sizes are placed. Following the example of [19], only the cylindrical inserts with a diameter of 12.5 mm were analysed. The investigated inserts consist of polymethylpentene (PMP), Teflon, polyoxymethylene (POM, also known as Delrin), Polystyrene, polyethylene (LDPE) and Acrylic. After reconstruction, the RSP was obtained in square-shaped regions of interest (ROIs) with a side length of 6 mm placed at the centre of each insert (figure 3).

2.3. Reconstruction and analysis

2.3.1. Forward projections and reconstruction

For each of the investigated setup geometries, 360 projections were recorded at 1 ° steps and used to reconstruct the RSP map inside the phantom. Per projection, the phantom was irradiated with 7.5×10^5 primary particles with a particle flux of ≈100 protons per mm^2. The obtained forward projections were further processed by applying standard 3σ cuts on kink angle and energy loss to eliminate large-angle scattering events [26]. Following the example of [19], the pCT image was reconstructed using distance-driven-binning (DDB) [27] and 1 mm^3 voxels with a slice thickness of 1 mm. DDB is a reconstruction algorithm for pCT which is based on filtered back-projection and approximates the particle's trajectory via most likely path (MLP) estimation [26].

2.3.2. Reference RSP

In contrast to [19], where the reference RSP ($\mathrm{RSP_{ref}}$) was taken from an actual residual range measurement in water [28], additional MC simulations of a residual range measurement were performed within this work to obtain $\mathrm{RSP_{ref}}$. The simulated setup consisted of an absorber with thickness t_m placed in front of a water block. The corresponding shift in residual range, defined by the shift in R20 (position in the water block, where the energy deposition has decreased to 20 % of its maximum), was measured

to estimate the water equivalent thickness (WET) [29] of each material. Then, $\mathrm{RSP_{ref}}$ was determined for each material by dividing the measured WET by the thickness t_m of the absorber ($\mathrm{WET} = \int \mathrm{RSP} \cdot dx \approx \mathrm{RSP} \cdot t_\mathrm{m}$). The main reason for using MC simulations to acquire the reference RSP values is the sensitivity of the RSP to the material definition in the simulation. For example, in [28] the measured reference RSP values were compared to a simulation which, depending on the material, yielded relative RSP differences up to 1.96 %. Therefore, since our study is solely based on MC simulations, the reference RSP values were taken from the simulated residual range measurement, which uses the same material composition and physics list as the pCT simulation.

2.3.3. RSP accuracy and precision

The RSP accuracy and precision were determined for each of the investigated TOF-pCT setups to study the influence of the individual system parameters. For that purpose, the RSP was collected in fifteen slices per ROI, as indicated in Figure 3. From the resulting RSP distributions, the median and mean μ_RSP of the RSP were obtained for each insert and compared to $\mathrm{RSP_{ref}}$. In order to quantify the RSP precision, the quartile coefficient of dispersion

$$\mathrm{QCOD_{RSP}} = \frac{\mathrm{Q_{3,RSP}} - \mathrm{Q_{1,RSP}}}{\mathrm{Q_{1,RSP}} + \mathrm{Q_{3,RSP}}}, \tag{11}$$

with $\mathrm{Q_{1,RSP}}$ and $\mathrm{Q_{3,RSP}}$ as the first and third quartiles of the RSP distribution, was determined for each insert. To estimate the overall RSP accuracy of the pCT scan, the mean absolute percentage error (MAPE) was calculated according to

$$\mathrm{MAPE} = \frac{\sum_i^{n_\mathrm{mat}} \epsilon_\mathrm{RSP,i}}{n_\mathrm{mat}}, \tag{12}$$

with $n_\mathrm{mat} = 6$ different inserts and

$$\epsilon_\mathrm{RSP} = \frac{|\mathrm{RSP_{ref}} - \mathrm{RSP_{meas}}|}{\mathrm{RSP_{ref}}} \tag{13}$$

as the relative error per insert. The measured QCOD and MAPE were then compared to an ideal pCT simulation, assuming infinitesimally thin sensors ($\mathrm{X/X_0} = 0$) and a perfect energy and position measurement. For the ideal setup, the input energy and the residual kinetic energy, which are both required for the reconstruction [27], were measured directly at the second tracker upstream of the phantom and the first tracker downstream of the phantom, respectively.

2.3.4. Imaging dose

The imaging dose was determined for every TOF-pCT setting using a Geant4 primitive dose scorer with a 1 mm × 1 mm × 1 mm dose grid, which was rotated together with the phantom. The absorbed dose was accumulated in every voxel of the dose grid to obtain the total dose distribution per pCT scan. Then, the median and interquartile range (IQR) of the corresponding dose distribution were calculated to estimate the imaging dose for each setting.

3. Results

3.1. Time-of-flight calorimeter

In this section, results showing the performance of a stand-alone TOF calorimeter for different system settings are presented. The goal is to identify and optimize the system parameters which dominate the energy measurement.

3.1.1. Energy resolution

Figure 4 shows the energy resolution obtained from a simulation of a realistic TOF calorimeter compared to the analytical model as described in equation (5). In addition,

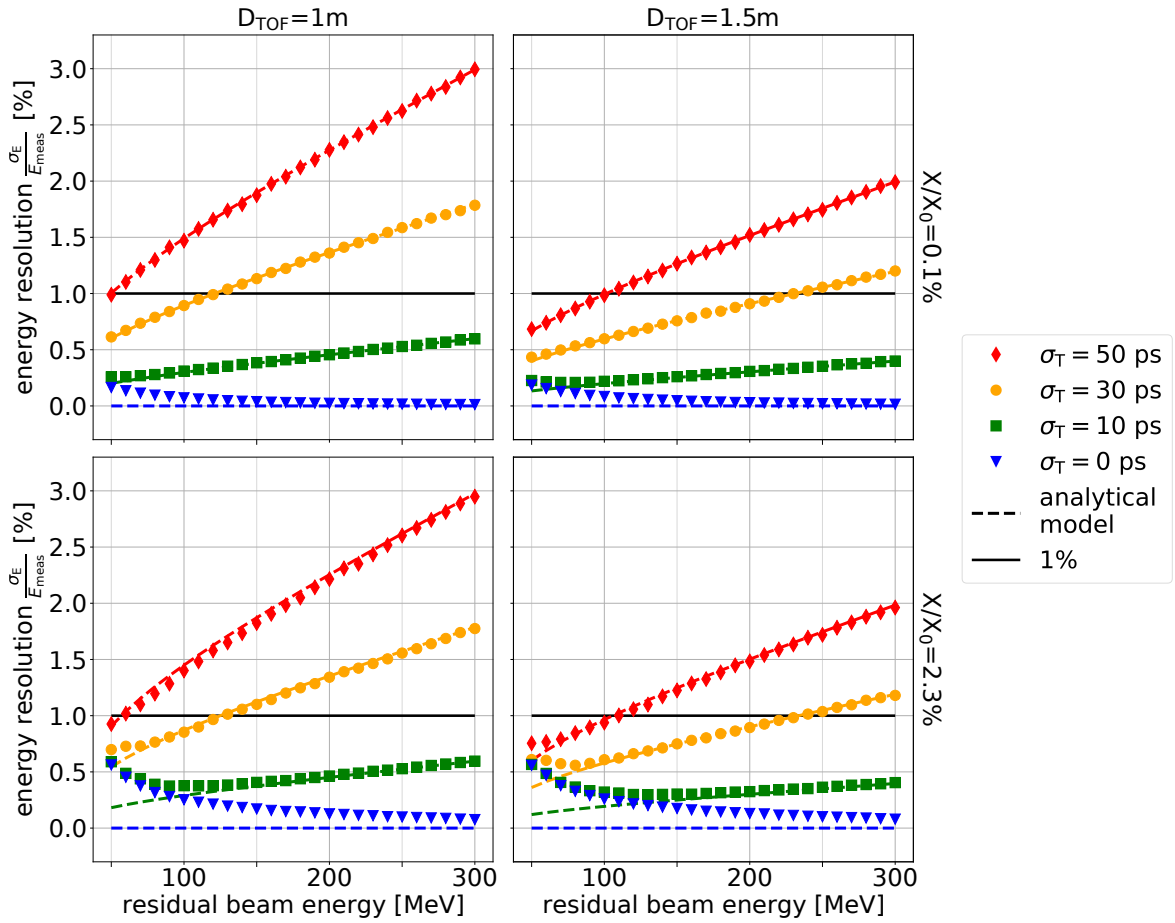

Figure 4: The energy resolution was simulated (diamond-shaped, circular and square markers) for different system parameters and compared to the analytical model (dashed lines) assuming $\sigma_L = 0$. Two material budgets, 0.1 % (top) and 2.3 % (bottom), and two flight distances, 1 m (left) and 1.5 m (right), were considered. For comparison, the 1 % requirement for a single-staged residual energy calorimeter [30] is also shown.

a simulation of an ideal TOF measurement with $\sigma_T = 0$ ps was performed for each setting to estimate the impact of energy straggling inside the calorimeter. As can be seen in figure 4, energy resolutions close to the straggling limit could be observed for $\sigma_T =$

10 ps and for beam energies $\leq$ 100 MeV. Also, for settings with more realistic intrinsic time resolutions $\geq$ 30 ps and X/X_0=2.3 %, energy straggling along the particle path has to be taken into account if residual beam energies $\leq$ 70 MeV are expected. For all other investigated settings, the precision of the energy measurement is well described by the analytical model as defined in equation (5). According to equation (5), the most dominating factors influencing the energy resolution are the intrinsic time resolution per tracking plane, flight distance and beam energy, which can also be observed in figure 4.

3.1.2. Accuracy and calibration of a realistic TOF calorimeter

The importance of an energy calibration for the TOF calorimeter can be seen when looking at figure 5, where the absolute error of the energy measurement is shown for different system settings. For an ideal setup with 0 ps time resolution, the absolute

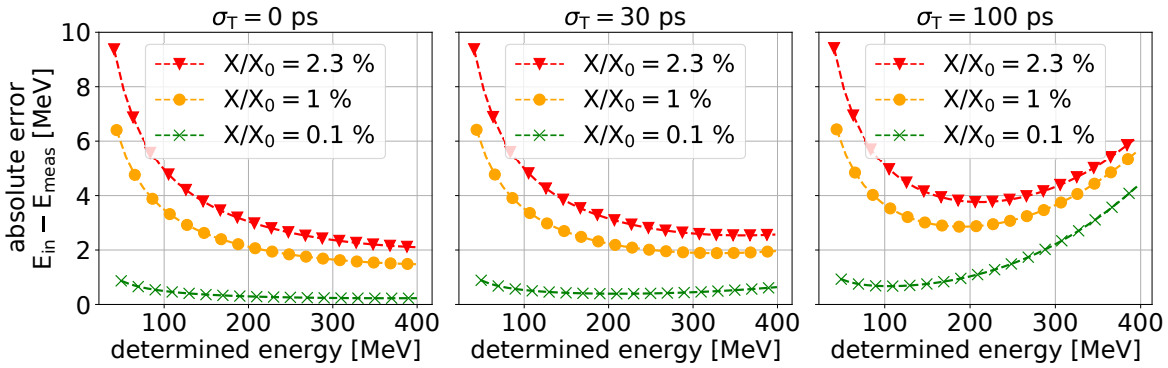

Figure 5: Simulated absolute error of the energy measurement for an LGAD based TOF calorimeter with a flight distance of 0.5 m, different material budgets, intrinsic time resolutions per tracker plane and determined residual proton energies (E_{meas}). For each setting a calibration curve was obtained, shown as the dashed lines.

error increases with increasing material budget per LGAD module and decreasing beam energy due to the significant energy loss inside the detectors. At higher beam energies, the energy loss decreases due to lower stopping power values, and therefore smaller absolute errors are expected. However, when realistic intrinsic time resolutions are assumed ($\geq$ 30 ps), an increase of the absolute error at higher beam energies can be observed. The reason for this increased inaccuracy at higher beam energies is shown in figure 6, where the distorted theoretical time-of-flight (section 2.1.4) is depicted for 800 MeV protons and a flight distance of 1 m (lower left). Since this effect is less pronounced at lower beam energies, 800 MeV protons were used to better illustrate this behaviour. As depicted in figure 6, due to the non-linear relation between TOF and kinetic energy (equation (3)), the most probable value (MPV) of the measured kinetic energy distribution (top left) is shifted towards lower beam energies if uncertainties of the TOF measurement are assumed (bottom right). For example, using 30 and 100 ps resulted in a shifted MPV (circles top left) of 797 MeV and 768 MeV, respectively.

In addition, the energy distribution is skewed, with a large tail towards higher beam energies.

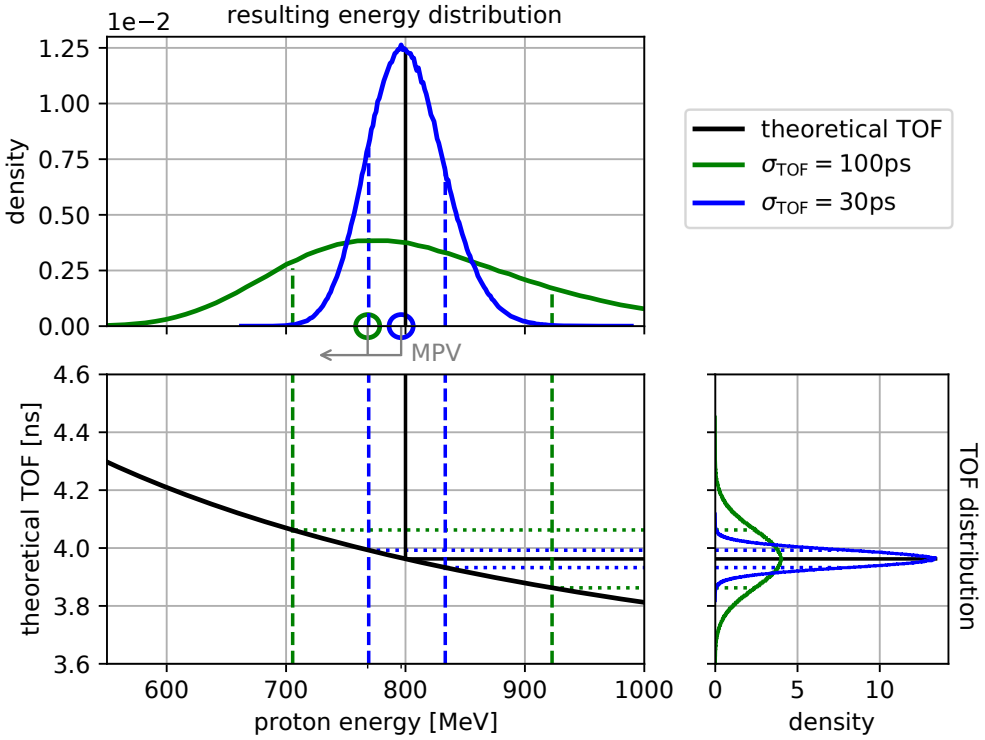

Figure 6: The influence of the intrinsic timing resolution per tracking plane on the energy measurement is shown for 800 MeV protons and a TOF path length of 1 m. The non-linear relation between TOF and energy (bottom left) results in an asymmetric shift of the energy distribution (top left) if high TOF uncertainties are assumed (bottom right). The most probable value of the energy distribution (MPV), indicated as circles (top left), is shifted towards lower beam energies with increasing σ_{TOF}. In order to highlight the asymmetry of the resulting energy distribution, the corresponding energies of the symmetric 1-σ interval of the TOF distribution (dotted lines) are shown as dashed lines.

After applying the calibration curves, highlighted as dashed lines in figure 5, to a new set of simulations, the relative error ϵ_E (equation (10)) was calculated for each TOF calorimeter configuration to estimate the accuracy of the energy measurement. For all investigated settings, only relative errors below 0.22 % could be observed. As an example, the obtained accuracy values for a TOF calorimeter with a flight distance of 0.5 m and different system parameters are shown in figure 7.

3.1.3. Influence of the spatial resolution

The influence of the intrinsic spatial resolution on the energy resolution and accuracy of a stand-alone TOF calorimeter was studied for σ_{xy} ranging from 0 mm to 5 mm. No impact of the spatial resolution on the performance of the energy measurement

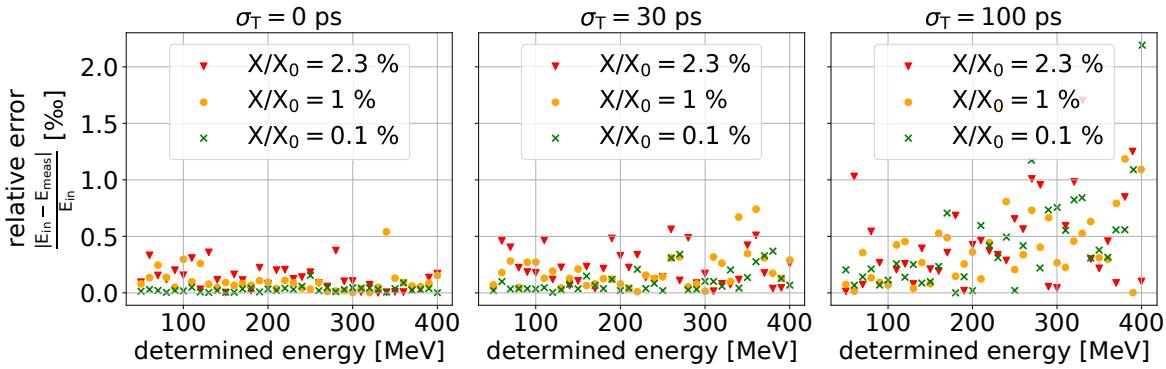

Figure 7: Accuracy of the energy measurement for an LGAD based TOF calorimeter after calibration. The relative error is shown for a setup with a flight distance of 0.5 m, different material budgets, intrinsic time resolutions per tracker plane and determined residual proton energies (E_{meas}).

could be observed for all investigated system settings. The accuracy and the energy resolution only differed by $\leq 0.05\,\%$ and $\leq 0.033\,\%$, respectively, when compared to $\sigma_{xy} = 0\,\text{cm}$. Consequently, the intrinsic spatial resolution should only affect the tracking performance of the proposed TOF-pCT system, which uses the same detector technology for particle tracking and residual energy measurements. The influence of the intrinsic spatial resolution of tracking detectors on the MLP estimation and achievable image voxel sizes has already been discussed extensively in [31, 32]. Therefore, since this work focuses on the TOF-based residual energy measurement, the spatial resolution was set to zero for all of the following simulations of different TOF-pCT systems.

3.2. Proton computed tomography system

As discussed in section 2.2.2, the RSP was measured inside the inserts of the CTP404 phantom to estimate the performance of the TOF-based pCT system. An example for the acquired RSP distributions per insert is shown in figure 8. Also, the theoretical RSP values, obtained via a simulated residual range measurement, are listed. The median and sample mean of the RSP are in good agreement with the reference RSP values.

3.2.1. RSP precision

Similar to the energy resolution of the TOF calorimeter, the RSP precision strongly depends on the intrinsic time resolution per tracking plane and the beam energy. This also becomes evident when looking at figure 9, where the central slices of the reconstructed CTP404 phantom are shown for 30 and 100 ps intrinsic time resolutions per tracking plane. The noise for $\sigma_T = 100\,\text{ps}$ (right) is increased in contrast to $\sigma_T = 30\,\text{ps}$ (left) due to the inferior intrinsic time resolution. With increasing beam energy and inferior intrinsic time resolutions, even more noise was observed in the central slices.

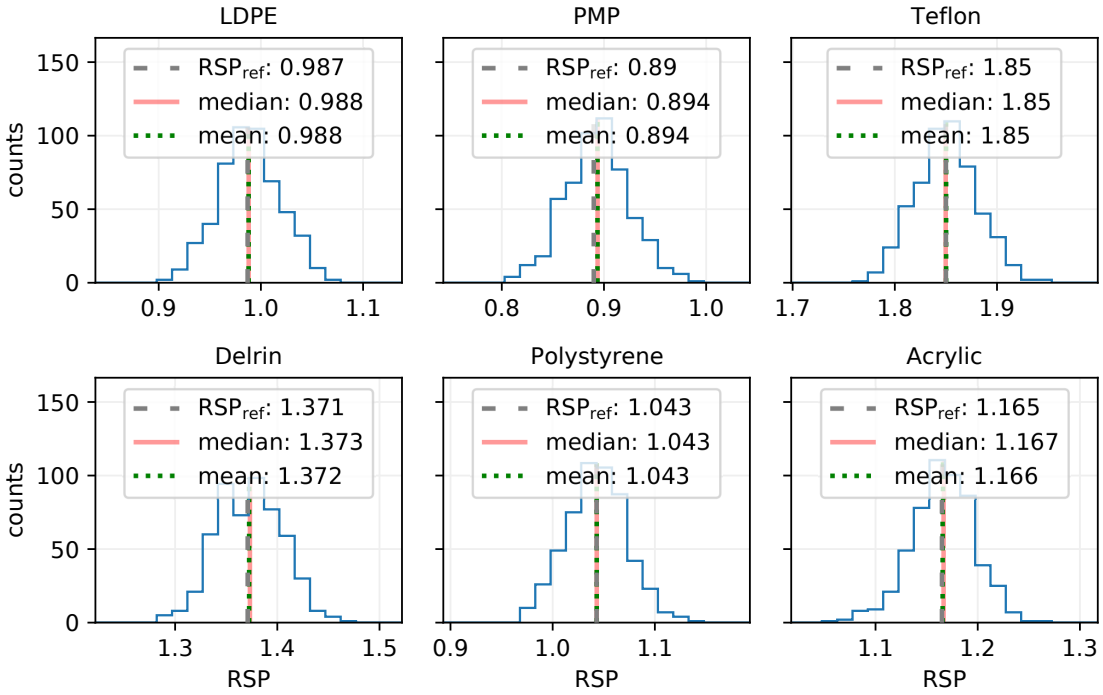

Figure 8: Collected RSP distributions in the CTP404 inserts (blue histograms) for 200 MeV protons, a flight distance of 1 m, 0.1 %X/X$_0$ and 30 ps σ_T per LGAD module. The sample RSP mean (dotted lines) and the RSP median (solid lines) are compared to reference RSP values (dashed lines). For almost all of the depicted inserts, the sample mean, median and reference value overlap.

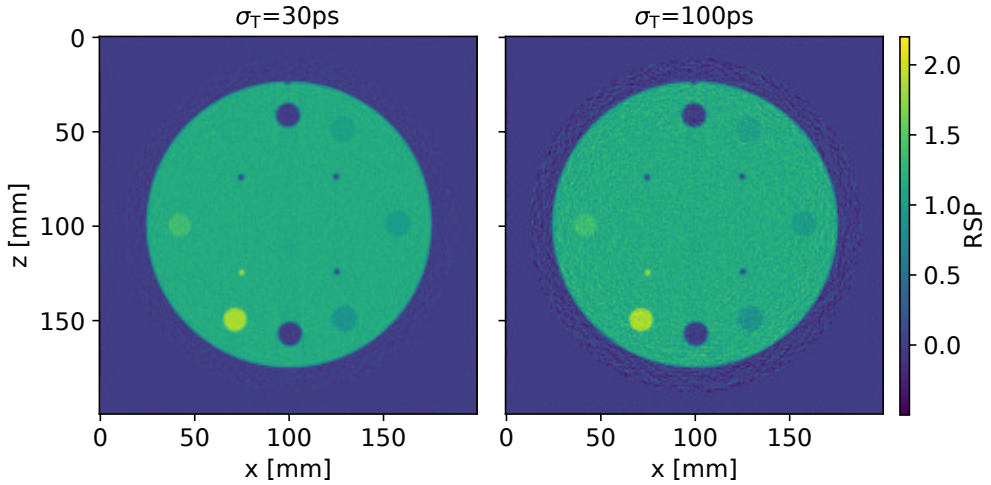

Figure 9: Reconstructed central slices of the CTP404 phantom recorded with 200 MeV protons and σ_T = 30 ps (left) and σ_T = 100 ps (right). The pixels outside the field of view (FOV) have been set to 0.

In order to quantify the RSP precision, the QCOD of the RSP was measured in each

insert. Figure 10 shows the corresponding QCOD for Teflon, obtained with a TOF-pCT system with a flight distance of 1 m, 0.1 % X/X_0 (left) and 2.3 % (right) X/X_0 in comparison to an ideal pCT simulation. Independent of the investigated setup,

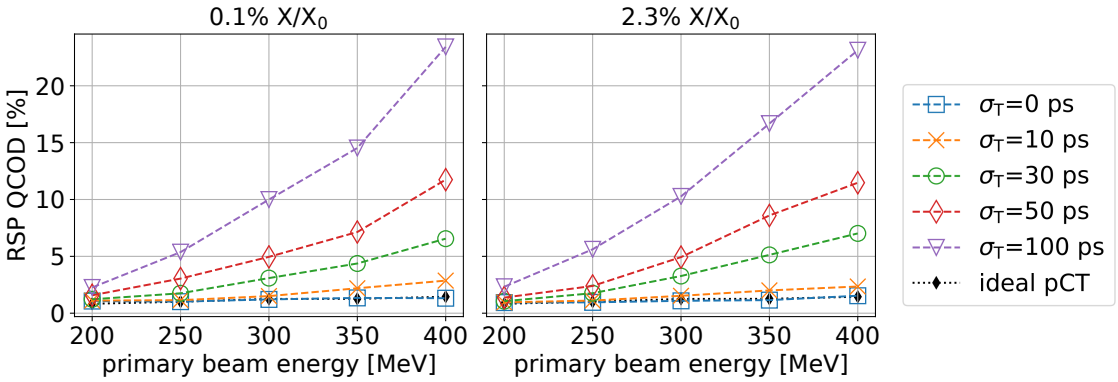

Figure 10: Energy dependence of the RSP precision measured in the Teflon insert. The RSP QCOD was calculated for different material budgets, intrinsic time resolutions per tracking plane with $D_{TOF} = 1$ m and compared to a simulation of an ideal pCT setup.

the RSP precision improves with decreasing beam energy and increased intrinsic time resolution. At $\sigma_T = 10$ ps, the QCODs are close to the values obtained from the ideal pCT simulation, where the RSP precision is only dominated by the straggling inside the phantom.

3.2.2. RSP accuracy

Figure 11 illustrates the measured RSP MAPEs for different pCT system parameters.

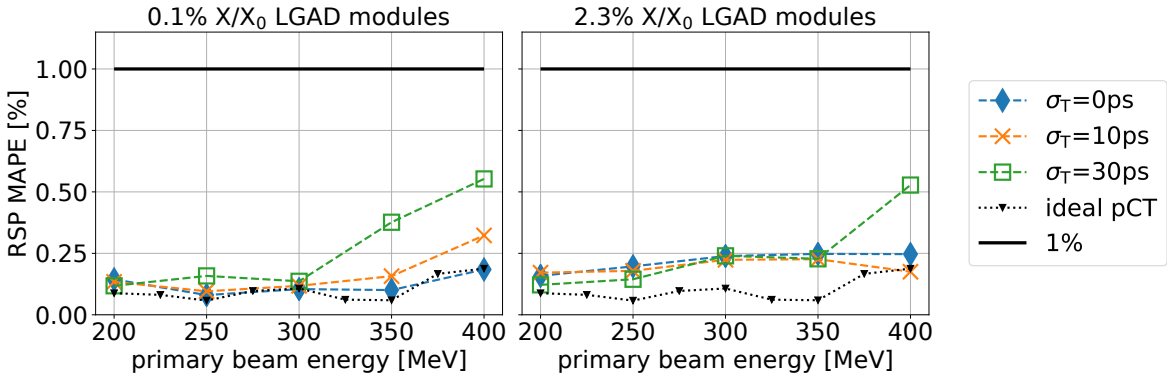

Figure 11: RSP MAPE for different material budgets and different intrisic time resolutions per tracking plane at $D_{TOF} = 1$ m. The MAPE was calculated for different primary beam energies and compared to a simulation of an ideal pCT setup. After calibrating the TOF-pCT systems, the MAPE was always well below the 1 % requirement [14] for all investigated settings.

For all investigated settings, the proposed calibration procedure allowed to achieve RSP accuracies close to the theoretical limit, defined by the simulation of the ideal pCT system. The obtained RSP MAPEs varied between 0.12 and 0.6 %, which is well below the requirements for a clinical pCT system [14]. Also, the lower limit of the obtained MAPE is in good agreement with the MAPE obtained from an ideal pCT system simulated in [19] and only differed by ≈ 0.1 %, which could result from a different estimation of the reference RSP values, as described in section 2.3.2. As depicted in figure 11, the ideal setup and the investigated TOF-pCT systems showed similar fluctuations in the obtained MAPE, which depend on the beam energy. Only for 0.1 % X/X_0, σ_T=30 ps and beam energies $\geq$ 350 MeV, considerable differences were observed, which could indicate a non-ideal energy calibration for those specific settings.

	ideal pCT	**TOF-pCT with σ_T = 30 ps**		
$\frac{X}{X_0}$ [%]	0	0.1	1	2.3
PMP	0.232 ± 0.119	0.410 ± 0.150	0.306 ± 0.158	-0.033 ± 0.160
LDPE	-0.004 ± 0.099	0.098 ± 0.162	0.177 ± 0.132	0.262 ± 0.153
Polystyrene	-0.030 ± 0.096	0.012 ± 0.122	0.007 ± 0.120	0.211 ± 0.135
Acrylic	0.035 ± 0.085	0.057 ± 0.113	0.162 ± 0.121	0.154 ± 0.133
Delrin	-0.330 ± 0.079	0.103 ± 0.099	0.074 ± 0.102	-0.008 ± 0.107
Teflon	-0.153 ± 0.055	0.011 ± 0.071	-0.007 ± 0.712	-0.202 ± 0.098
MAPE [%]	**0.081**	**0.115**	**0.122**	**0.145**

Table 2: Relative RSP errors [%] of the pCT system for 200 MeV protons, a flight distance of 1m and an intrinsic time resolution of 30 ps. The standard error of the mean was used to estimate the uncertainty of the RSP accuracy in each insert.

For a more detailed comparison of the investigated TOF-pCT setups, the relative RSP errors per insert, the standard errors of the mean, as well as the MAPEs are listed in table 2 for TOF-pCT systems with 30 ps intrinsic time resolution, different material budgets per LGAD module and a primary beam energy of 200 MeV.

3.2.3. Imaging dose

Decreasing the primary beam energy resulted in higher imaging doses. The pCT scans at 400 MeV yielded the lowest imaging dose with a median of 1.86 mGy and an IQR of 0.36 mGy. At 200 MeV, the median and IQR of the imaging dose distribution increased to 2.89 mGy and 0.55 mGy, respectively. For each energy, the variation between the individual TOF-pCT settings was less than 0.3 %.

4. Discussion

The aim of this work was to investigate the feasibility of a pCT system based on 4D-tracking detectors with a TOF calorimeter for the residual energy measurement, which,

so far, does not exist. The authors of [17] have reported first design efforts towards a TOF-based proton computed radiography system consisting of micro channel plate photomultiplier tubes (MCPT) with an intrinsic time resolution of 64 ps and a spatial resolution of 1 mm^2. However, no TOF-based energy measurement could be achieved with the presented MPCT scanner. LGADs, on the other hand, have already been successfully employed as beam monitors for ion beam therapy [15]. Since LGADs are also an emerging detector technology with promising intrinsic timing and spatial resolution, we exclusively focussed on LGAD-based TOF-pCT systems. Several design parameters were studied and optimized using a realistic Geant4 model of the TOF-pCT scanner. In general, the proposed pCT system could also be used for other ion species. The advantages of using a TOF system for He-CT have already been discussed in [18, 16]. For example, in [18], the performance of a theoretical TOF-based residual energy calorimeter for helium ion computed tomography (HeCT) has been studied in terms of RSP resolution. The authors of [16], on the other hand, have shown that measuring the TOF through the patient could be used for particle identification to remove nuclear interaction events. However, since investigating other ions species would go beyond the scope of this study, we have only presented the results for a TOF-based proton computed tomography system.

4.1. Impact of the investigated system parameters on the energy measurement

The performance of a stand-alone TOF-based residual energy calorimeter has been investigated in terms of precision and accuracy.
To achieve WET resolutions close to the theoretical range straggling limits, the energy resolution of a residual energy calorimeter (single staged) for pCT should be $< 1\,\%$ for residual energies ranging from a few tens of MeV to a few hundreds of MeV [30]. Thus, it was necessary to identify and discuss the design parameters that influence the energy resolution of the TOF calorimeter prior to designing a realistic pCT system based on 4D-tracking detectors. Similar results as described in [18] were found, where the influence of the intrinsic time resolution and flight distance of a TOF calorimeter on the precision of an ion CT with 200 MeV/u He-ions was studied. The study presented in this work, on the other hand, also investigated the influence of spatial resolution, material budget, and different residual beam energies for a more comprehensive analysis, which should serve as a guide for future hardware developments. As indicated in figure 4, the energy resolution improves with decreasing residual beam energy down to ≈ 100 MeV for all investigated settings. However, at lower energies, depending on the setting, a significant contribution due to increased energy straggling inside the TOF calorimeter could be observed. Therefore, to fully optimize the residual beam energy for each setting, a simulation of the calorimeter setup should be preferred over the analytical model (equation (5)), where energy straggling was not taken into account. The energy resolution is also strongly impacted by the intrinsic time resolution per plane. In general, LGADs with the most precise intrinsic time resolution should be used for the TOF

calorimeter to improve the energy resolution. Recent studies have shown that time resolutions of $\approx 30\,\mathrm{ps}$ can be achieved [5]. For an LGAD based TOF calorimeter with $\sigma_\mathrm{T} = 30\,\mathrm{ps}$ and a flight distance of 1 m, residual energies should be $\leq 100\,\mathrm{MeV}$ in order to reach the desired energy resolutions below the 1 % limit. Alternatively, longer flight distances could be used for the same intrinsic time resolution when higher residual beam energies are expected.
The energy loss inside the detector modules and the intrinsic time resolution have been identified as the main sources of inaccuracy for the energy measurement. In order to account for those inaccuracies, a dedicated calibration procedure has been introduced. After applying the calibration, the relative error of the energy measurement could be decreased to $\approx 0.2\,\%$ for all settings. Within the investigated parameter space, no significant influence of the flight distance, beam energy, material budget or intrinsic time resolution on the accuracy of the energy measurement could be observed after the calibration.
Another important design aspect is the granularity of the 4D-tracking detector. The concept of high-granularity detectors for pCT has already been introduced in [33] to cope with the high particle rates of clinical pencil beams. Using detectors with high granularity reduces the sensor occupancy since fewer particles will traverse the same detector cell at the same time. This allows recording a high multiplicity of incoming particle tracks, which results in an increased rate capability. Within this work, we investigated whether additional limitations on the granularity have to be imposed in terms of required spatial resolution for the residual energy measurement. However, for $\sigma_{xy} < 5\,\mathrm{mm}$, no significant influence on the performance of the energy measurement could be observed. Consequently, the design choice for the sensor granularity of the LGAD based TOF-pCT system is mainly driven by the required image voxel size [31, 32] and rate capability of the 4D-tracking system.

4.2. Impact of the investigated system parameters on the RSP determination

As described in [14], a clinical pCT system should be able to measure the RSP inside $\leq 1\,\mathrm{mm}^3$ voxels with an accuracy better than 1 %. Those requirements have already been fulfilled by the phase II preclinical pCT prototype scanner [34], which achieved RSP accuracies of $\approx 0.69\,\%$ [19]. To show the potential of pCT to further improve the RSP accuracy, the authors of [19] have also simulated an ideal pCT system with infinitesimally thin detectors and ideal energy and position measurements, which reached RSP accuracies down to $\approx 0.17\,\%$. Following the example of [19], we also simulated an ideal pCT system for verification and for comparing the performance of the realistic TOF-based pCT scanner. Similar to the stand-alone TOF calorimeter, no significant dependence on any system parameter on the RSP accuracy was observed after applying the calibration as described in the previous sections. Only for higher beam energies, using higher material budgets, the MAPE increased up to 0.6 %, which is still well below the 1 % margin. The best RSP accuracy (0.12 %) was obtained for a pCT

system with 0.1 %X/X_0 LGADs, a flight distance of 1 m and intrinsic time resolution of 30 ps, which is close to the theoretical limit defined by the ideal pCT simulation (table 2). The promising improvements in terms of RSP accuracy indicate that a TOF-based pCT scanner could outperform the latest dual-energy CT (DECT) scanners used for treatment planning, which achieved RSP accuracies $\gtrapprox 0.6\,\%$ [35, 36, 19]. This, however, has to be confirmed with an experimental prototype.

Figure 4 suggests that if 10 ps intrinsic time resolution per LGAD is assumed, the resulting WET resolution should be close to the theoretical straggling limit, independent of the investigated flight distances and residual beam energies. Similarly, the RSP precision was also always close to the results obtained from the ideal pCT simulation if σ_T was set to 10 ps. Assuming a more realistic intrinsic time resolution (e.g. 30 ps) resulted in a significant decrease of RSP precision as indicated in figure 10. However, it is important to mention that the design parameters of the investigated TOF-pCT systems were not fully optimized to boost the RSP precision. For example, increasing the flight distance of the TOF calorimeter could also further improve the energy resolution and, therefore, the RSP precision. In a clinical environment, however, the flight distance cannot be set arbitrarily large due to the already limited space in the treatment room. Alternatively, as indicated in equation (6), more LGADs could be used per timing station to improve the RSP precision. Since this would increase the cost of the pCT system, optimizing the other system parameters should be preferred. In general, for a realistic LGAD system with $\sigma_T \geq 30$ ps and $D_{TOF} \leq 1$ m, the residual beam energy should be kept as low as possible, as indicated in figure 4. This also implies that TOF-pCT would greatly benefit from an energy-modulated beam to account for a varying phantom thickness. The concept of using an energy-modulated beam for pCT to improve the image noise has already been studied in [37] and could equally be applied to a TOF-pCT system, which, however, is outside the scope of this study.

4.3. Impact of the investigated system parameters on the image dose

No significant impact of the investigated system parameters on the imaging dose ($\leq 0.3\,\%$) could be observed. As expected, the delivered dose per scan increased with decreasing beam energy. The obtained imaging doses for the pCT scans with 200 MeV were ≈ 2.89 mGy, which is slightly higher when compared to the simulation results from the phase II preclinical pCT prototype scanner [19] where an imaging dose between 1.6 mGy and 1.9 mGy was reported for the same phantom, beam energy and the total number of primary particles. A possible explanation for this discrepancy could be a different particle flux, which, however, was not specified in [19]. Nevertheless, the resulting doses per TOF-pCT scan were still considerably lower than the typical doses obtained with conventional SECT and DECT (> 10 mGy [19, 38, 39]) and could be even further reduced by, for example, using a fluence-modulated beam [40, 41].

5. Conclusion

The main purpose of this study was to offer a comprehensive overview of the most important system parameters of a realistic TOF-pCT scanner based on 4D-tracking detectors, serving as a guide for future hardware developments. Using MC simulations, we could demonstrate that a TOF-based pCT system could potentially achieve RSP accuracies well below the 1 % margin, if properly calibrated, and therefore improve the treatment plan quality. Using a model of a realistic TOF-pCT setup with 1 % X/X_0, 30 ps intrinsic time resolution and a flight distance of 1 m resulted in an RSP accuracy of ≈ 0.12 %, which could outperform the latest DECT scanners (≈ 0.6 %). To achieve an RSP resolution close to the straggling limit, intrinsic time resolutions of at least 30 ps are recommended. However, for a more realistic setup with time resolutions ≥ 30 ps, system parameters such as residual beam energy, flight distance and number of LGADs should be optimized to further improve the RSP precision.

Acknowledgements

This project received funding from the Austrian Research Promotion Agency (FFG), grant number 869878.

References

[1] The ATLAS Collaboration. Technical Proposal: A High-Granularity Timing Detector for the ATLAS Phase-II Upgrade. `https://cds.cern.ch/record/2623663`. Accessed: 2021-12-01.

[2] CMS Collaboration. A MIP Timing Detector for the CMS Phase-2 Upgrade. `https://cds.cern.ch/record/2667167`. Accessed: 2021-12-01.

[3] J Pietraszko, T Galatyuk, V Kedych, and M Kis others. Low gain avalanche detectors for the HADES reaction time (T_0) detector upgrade. *Eur. Phys. J. A*, 56(7), 2020.

[4] N Cartiglia, R Arcidiacono, G Borghi, M Boscardin, et al. LGAD designs for Future Particle Trackers. *NIM A*, 979:164383, 2020.

[5] N Cartiglia, A Staiano, V Sola, R Arcidiacono, et al. Beam test results of a 16ps timing system based on ultra-fast silicon detectors. *NIM A*, 850:83–88, 2017.

[6] M Tornago, R Arcidiacono, N Cartiglia, M Costa, et al. Resistive AC-coupled silicon detectors: Principles of operation and first results from a combined analysis of beam test and laser data. *NIM A*, 1003:165319, 2021.

[7] E Currás, M Carulla, M C Vignali, J Duarte-Campderros, et al. Inverse low gain avalanche detectors (iLGADs) for precise tracking and timing applications. *NIM A*, 958:162545, 2020.

[8] R P Johnson. Review of medical radiography and tomography with proton beams. *Rep. Prog. Phys.*, 81(1):016701, 2017.

[9] S Meyer, F Kamp, T Tessonnier, A Mairani, et al. Dosimetric accuracy and radiobiological implications of ion computed tomography for proton therapy treatment planning. *PMB*, 64(12):125008, 2019.

[10] M Scaringella, M Bruzzi, M Bucciolini, M Carpinelli, et al. A proton computed tomography based medical imaging system. *JINST*, 9(12):C12009–C12009, 2014.

[11] H E S Pettersen, J Alme, G G Barnaföldi, R Barthel, et al. Design optimization of a pixel-based range telescope for proton computed tomography. *Phys. Med.*, 63:87–97, 2019.

[12] M Esposito, C Waltham, J T Taylor, S Manger, et al. PRaVDA: The first solid-state system for proton computed tomography. *Phys. Med.*, 55:149–154, 2018.

[13] HF-W Sadrozinski, R P Johnson, S Macafee, A Plumb, et al. Development of a head scanner for proton CT. *NIM A*, 699:205–210, 2013.

[14] R Schulte, V Bashkirov, L Tianfang, L Zhengrong, et al. Conceptual design of a proton computed tomography system for applications in proton radiation therapy. *IEEE Trans. Nucl. Sci.*, 51(3):866–872, 2004.

[15] A Vignati, S Giordanengo, F Mas Milian, Z Ahmadi Ganjeh, et al. A new detector for the beam energy measurement in proton therapy: a feasibility study. *PMB*, 65(21):215030, 2020.

[16] M Rovituso, C Schuy, U Weber, S Brons, et al. Fragmentation of 120 and 200 MeV u-14he ions in water and PMMA targets. *PMB*, 62(4):1310–1326, 2017.

[17] W A Worstell, B W Adams, M Aviles, J Bond, et al. First results developing time-of-flight proton radiography for proton therapy applications. In *Medical Imaging 2019: Physics of Medical Imaging*, volume 10948, pages 101 – 109. SPIE, 2019.

[18] L Volz. *Particle imaging for daily in-room image guidance in particle therapy*. PhD thesis, Heidelberg University, 2021.

[19] G Dedes, J Dickmann, K Niepel, P Wesp, et al. Experimental comparison of proton CT and dual energy x-ray CT for relative stopping power estimation in proton therapy. *PMB*, 64(16):165002, 2019.

[20] S Agostinelli, J Allison, K Amako, J Apostolakis, et al. Geant4—a simulation toolkit. *NIM A*, 506(3):250–303, 2003.

[21] Mukund Gupta. Calculation of radiation length in materials. Technical report, CERN, Geneva, 2010.

[22] P A Zyla, R M Barnett, J Beringer, O Dahl, et al. Review of particle physics. *Prog. Theor. Exp. Phys.*, 2020(8), 2020.

[23] F Tosello. SDD Materials G10-FR4. `http://personalpages.to.infn.it/~tosello/EngMeet/ITSmat/SDD/SDD_G10FR4.html`. Accessed: 2021-06-01.

[24] M. Carulla, A. Doblas, D. Flores, Z. Galloway, et al. 50 µm thin Low Gain Avalanche Detectors (LGAD) for timing applications. *NIM A*, 924:373–379, 2019.

[25] UCSC LGAD readout board. `https://twiki.cern.ch/twiki/bin/view/Main/UcscSingleChannel`. Accessed: 2021-09-1.

[26] R W Schulte, S N Penfold, J T Tafas, and K E Schubert. A maximum likelihood proton path formalism for application in proton computed tomography. *Medical Physics*, 35(11):4849–4856, 2008.

[27] S Rit, G Dedes, N Freud, D Sarrut, et al. Filtered backprojection proton CT reconstruction along most likely paths. *Med. Phys.*, 40(3):031103, 2013.

[28] V Giacometti, V A Bashkirov, P Piersimoni, S Guatelli, et al. Software platform for simulation of a prototype proton CT scanner. *Med. Phys.*, 44(3):1002–1016, 2017.

[29] R Zhang and W D Newhauser. Calculation of water equivalent thickness of materials of arbitrary density, elemental composition and thickness in proton beam irradiation. *PMB*, 54(6):1383–1395, 2009.

[30] V A Bashkirov, R W Schulte, R F Hurley, R P Johnson, et al. Novel scintillation detector design and performance for proton radiography and computed tomography. *Med. Phys.*, 43(2):664–674, 2016.

[31] N Krah, F Khellaf, J M Létang, S Rit, et al. A comprehensive theoretical comparison of proton imaging set-ups in terms of spatial resolution. *PMB*, 63(13):135013, 2018.

[32] A Burker, T Bergauer, A Hirtl, C Irmler, et al. Single particle tracking uncertainties in ion imaging, 2021. arXiv:2008.08422.

[33] J Alme, G Gábor Barnaföldi, R Barthel, V Borshchov, et al. A high-granularity digital tracking calorimeter optimized for proton CT. *Front. Phys.*, 8, 2020.

[34] R P Johnson, V A Bashkirov, G Coutrakon, V Giacometti, et al. Results from a prototype

proton-ct head scanner. *Phys. Procedia*, 90:209–214, 2017.

[35] P Wohlfahrt, C Möhler, K Stützer, S Greilich, et al. Dual-energy CT based proton range prediction in head and pelvic tumor patients. *Radiother. Oncol.*, 125(3):526–533, 2017.

[36] N Hudobivnik, F Schwarz, T Johnson, L Agolli, et al. Comparison of proton therapy treatment planning for head tumors with a pencil beam algorithm on dual and single energy CT images. *Med. Phys.*, 43(1):495–504, 2016.

[37] J Dickmann, C Sarosiek, V Rykalin, M Pankuch, et al. Proof of concept image artifact reduction by energy-modulated proton computed tomography (EMpCT). *Phys. Med.*, 81:237–244, 2021.

[38] M J Murphy, J Balter, S Balter, J A BenComo, et al. The management of imaging dose during image-guided radiotherapy: Report of the AAPM Task Group 75: Imaging dose during image-guided radiotherapy. *Med. Phys.*, 34(10):4041–4063, 2007.

[39] G Landry, M Gaudreault, W van Elmpt, J E Wildberger, et al. Improved dose calculation accuracy for low energy brachytherapy by optimizing dual energy CT imaging protocols for noise reduction using sinogram affirmed iterative reconstruction. *Z. Med. Phys.*, 26(1):75–87, 2016.

[40] J Dickmann, S Rit, M Pankuch, R P Johnson, et al. An optimization algorithm for dose reduction with fluence-modulated proton CT. *Med. Phys.*, 47(4):1895–1906, 2020.

[41] G Dedes, R P Johnson, M Pankuch, N Detrich, et al. Experimental fluence-modulated proton computed tomography by pencil beam scanning. *Med. Phys.*, 45(7):3287–3296, 2018.